Supplementary Materials

Estimation of absolute stress in the hypocentral region of the 2019 Ridgecrest, California, earthquakes

Yuri Fialko

Contents

Online data

Focal mechanism catalog for Southern California is available at `https://scedc.caltech.edu/research-tools/alt-2011-yang-hauksson-shearer.html`, last accessed July 2020.

Waveform-relocated earthquake catalog for Southern California is available at `https://scedc.caltech.edu/research-tools/alt-2011-dd-hauksson-yang-shearer.html`, last accessed July 2020.

First motion focal mechanism of the 2019 M7.1 mainshock is available at
https://earthquake.usgs.gov/earthquakes/eventpage/ci38457511/focal-mechanism, last accessed July 2020.

Seismic moment of the 2019 M7.1 mainshock is available at
https://earthquake.usgs.gov/earthquakes/eventpage/ci38457511/moment-tensor, last accessed July 2020.

Seismic moment of the 2019 M6.4 foreshock is available at
https://earthquake.usgs.gov/earthquakes/eventpage/ci38443183/moment-tensor, last accessed July 2020.

Matlab utility used for plotting earthquake focal mechanisms is available at
https://www.mathworks.com/matlabcentral/fileexchange/61227-focalmech-fm-centerx-cente
last accessed July 2020.

Methods

To identify a population of active faults at seismogenic depths, I use a refined catalog of earthquake focal mechanisms for southern California with earthquake locations derived from waveform cross-correlation[1]. The catalog data for the Ridgecrest-Coso area (Figure 1) include around 3.2×10^4 focal mechanisms for earthquakes that occurred between January 1981 and July 2019. The orientation of seismically active faults is evaluated using a two-step procedure. Seismicity on sub-vertical strike-slip faults in the map view is manifested by lineated clusters of epicenters (see Figure S1). I use an unsupervised learning algorithm OPTICS (Ordering Points To Identify the Clustering Structure) to select clusters of events that satisfy prescribed criteria of proximity and density[2]. An event epicenter is selected as a core point of a cluster if it has a number of neighbors equal to or greater than 14. The search algorithm is executed iteratively, with an increasing distance that defines neighbors within a cluster, from 0.5 to 1.5 km. At the end of each iteration selected clusters are removed from the catalog and the search continues. This allows for selection of relatively small clusters in the neighborhood of larger ones. Clusters chosen by the OPTICS algorithm can have diverse geometries that are not necessarily linear. To select clusters that have a quasi-linear shape, and estimate the best-fit linear trends, I use RANSAC (Random Sample Consensus)[3] and robust linear regression algorithms. Application of the above procedure to the Ridgecrest data resulted in selection of 65 quasi-linear clusters, shown in Figures 1 and S2-S4. I note that the method can be extended to three dimensions to include dip-slip faults, in which case faults can be identified by seeking clusters of hypocenters that can be approximated by a plane (in 3D), or a line in a suitably chosen projection. Another possibility is to employ deep learning algorithms trained on synthetic catalogs.

For each of the linear fits to the scattered epicenter locations (red lines and black dots in Figures S2-S4), I estimate errors in the best-fit strike angle by computing deviation of the least-square linear fits treating northing and easting coordinates as independent variables[4]. The respective errors are shown as red numbers for each cluster in Figures S2-S4. On average the estimated uncertainties in fault strikes are on the order of several degrees. In a few cases when uncertainties exceed 10 degrees, they tend to reflect imperfect selection of data points by the clustering algorithm, rather than a wide range of possible fault strikes (e.g., Figures S2j, S2t, S3d, S3h, S4b, S4k).

To determine the sense of slip on the identified fault segments, I use focal mechanisms of events in the respective clusters. For each event I compute components of the seismic moment tensor M_{ij} from the magnitude (M_w), strike, dip, and rake angles provided in the focal mechanism catalog, $M_{ij} = M_0(u_i n_j + u_j n_i)$, where $M_0 = 10^{1.5M_w+10.7}$ is the scalar seismic moment in newton meters, n_i is the normal to a slip plane (defined by the strike and dip angles), and u_i is the unit slip vector (defined by n_i and the rake angle). I then compute a tensorial sum $\Sigma_k M_{ij}$, where k is a number of events in a cluster. To investigate the effect of diversity of focal mechanisms (e.g., to avoid a possible dominance of a largest event in a cluster), I also use moment tensors normalized by the scalar moment, $\bar{M}_{ij} =$

$M_{ij}/\sqrt{M_{mn}M_{mn}/2}$ (repeated indecies imply summation). Using original and normalized moment tensors gives rise to essentially the same results.

The composite moment tensors may have a significant non-double-couple component if focal mechanisms of events in a cluster are highly diverse. Yet the orientations of P and T axes (that determine the sense of slip on a plane defined by a seismicity lineation) are well resolved. The focal mechanisms shown in Figures 1, S2, S3, and S4 represent the best-fit double couple solutions for the composite moment tensors $\Sigma_k \bar{M}_{ij}$.

Uncertainties in the distribution of dihedral angles of conjugate faults (Figure 3) are estimated using uncertainties in individual fault strikes. Suppose e_i is uncertainty in the slope of a best linear fit for a cluster i, and m is a number of clusters in a given bin of dihedral angles, $2\theta_j < 2\theta < 2\theta_{j+1}$. The standard error of the mean of m angles is $\epsilon_j = s/\sqrt{m}$, where s is the standard deviation of $e_1, e_2, ..., e_m$ samples[5]. Uncertainties on a number of conjugate pairs for a given bin of dihedral angles are calculated by perturbing the upper and lower bound of a bin by $\pm\epsilon_j/2$ (i.e., $2\theta_j - \epsilon_j/2 < 2\theta < 2\theta_{j+1} + \epsilon_j/2$), and differencing the number of samples in an expanded bin and the original bin.

Given a stress field with axes of the effective principal stresses σ_1' and σ_3' parallel to the Earth's surface, a condition for activation of pre-existing strike-slip faults is[6,7]

$$R = \frac{\sigma_1'}{\sigma_3'} = \frac{1 + \mu_1 \cot\theta}{1 - \mu_1 \tan\theta}, \tag{1}$$

where R is the effective stress ratio, μ_1 is the coefficient of friction, and θ is the angle between a fault plane and the maximum compression axis. Expression (1) assumes a Mohr-Coulomb failure criterion, vertical orientation of the intermediate principal stress, and negligible (compared to friction) cohesion on a potential slip plane. In case of the Ridgecrest seismicity, all three unknowns (σ_1', σ_3', and μ_1) in equation (1) can be determined by making use of the following constraints: (i) the maximum compressive stress is close to lithostatic, as discussed in the main text, (ii) faults are activated when $\theta \approx \theta_1$, and (iii) faults are de-activated when

$\theta \approx \theta_2$ (see Figure 3 in the main text). A failure envelope $\tau = \mu_1 \sigma_n$, where τ and σ_n are the shear and normal stress resolved on a fault, intersects the Mohr circle at points corresponding to fault orientations $2\theta_1$ and $2\theta_2$ (see Figure 4) if

$$\mu_1 = \frac{1}{\tan(\theta_1 + \theta_2)}, \tag{2}$$

i.e., when the angle maximizing stress excursion beyond the failure envelope is given by an average of the activation and de-activation angles θ_1 and θ_2. Substituting equation (2) into equation (1), and taking θ to be equal to either θ_1 or θ_2, one obtains expressions for the effective stress ratio R and the effective minimum compressive stress σ'_3 provided in the main text.

For the prescribed principal stresses σ'_1 and σ'_3, one can use a relationship between the stress ratio and the coefficient of friction μ_0 that corresponds to an optimal orientation[6]

$$R = \left(\sqrt{1+\mu_0^2} + \mu_0\right)^2. \tag{3}$$

Solving for real non-negative values of μ_0, one obtains

$$\mu_0 = \frac{R-1}{2\sqrt{R}}. \tag{4}$$

References

1 Yang, W., Hauksson, E. & Shearer, P. M. Computing a large refined catalog of focal mechanisms for southern California (1981–2010): Temporal stability of the style of faulting. *Bull. Seism. Soc. Am.* **102**, 1179–1194 (2012).

2 Ankerst, M., Breunig, M. M., Kriegel, H.-P. & Sander, J. Optics: ordering points to identify the clustering structure. *ACM Sigmod record* **28**, 49–60 (1999).

3 Hast, A., Nysjö, J. & Marchetti, A. Optimal RANSAC-towards a repeatable algorithm for finding the optimal set (2013).

4 Fialko, Y. Evidence of fluid-filled upper crust from observations of post-seismic deformation due to the 1992 M_w7.3 Landers earthquake. *J. Geophys. Res.* **109**, B08401, 10.1029/2004JB002985 (2004).

5 Hogg, R. V., McKean, J. & Craig, A. T. *Introduction to mathematical statistics, 6th edition* (Pearson Education, 2005).

6 Sibson, R. H. A note on fault reactivation. *J. Struct. Geol.* **7**, 751–754 (1985).

7 Sibson, R. H. Rupture nucleation on unfavorably oriented faults. *Bull. Seism. Soc. Am.* **80**, 1580–1604 (1990).

8 Hauksson, E., Yang, W. & Shearer, P. M. Waveform relocated earthquake catalog for Southern California (1981 to 2011). *Bull. Seism. Soc. Am.* **102**, 2239–2244 (2012).

9 Jennings, C. & Bryant, W. Fault Activity Map of California (2010). California Division of Mines and Geology, Geologic Data Map No. 6.

10 DuRoss, C. B. *et al.* Surface displacement distributions for the July 2019 Ridgecrest, California, earthquake ruptures. *Bull. Seism. Soc. Am.* **110**, 1400–1418 (2020).

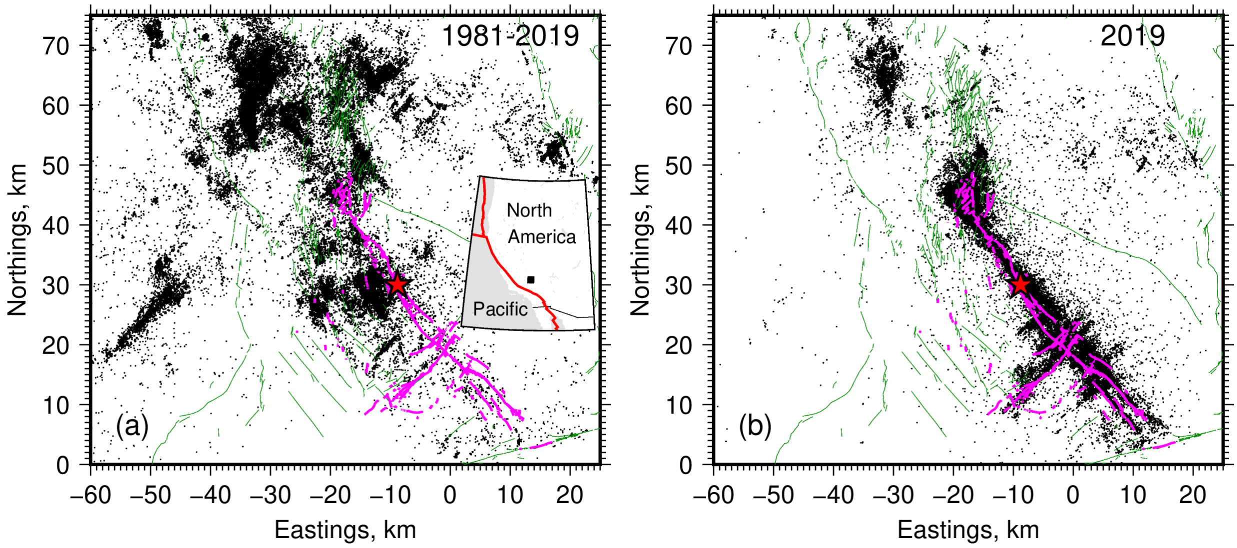

Figure S1: (a) Precisely relocated seismicity in the Ridgecrest-Coso area over a time period 1981-July 2019[8]. Thin green lines denote Quaternary faults[9]. Magenta lines denote surface traces of the 2019 ruptures[10]. Red star denotes the epicenter of the 2019 M7.1 earthquake. Inset shows the location of the study area. (b) Precisely relocated seismicity over 6 months following the July 2019 M7.1 event. Local origin is at 117.5°W, 35.5°N.

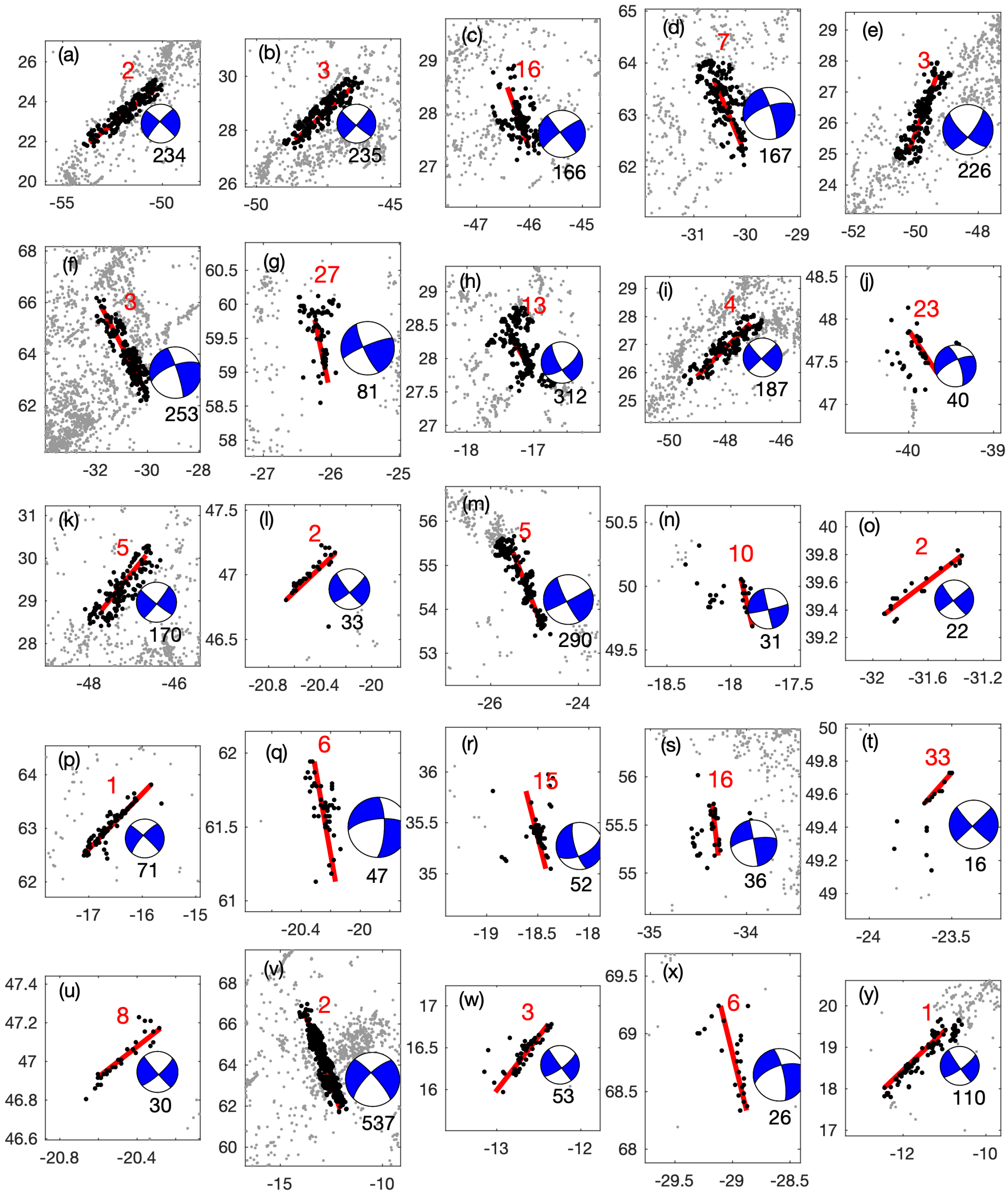

Figure S2: Seismicity lineations identified by the clustering algorithm. Grey dots denote the background seismicity, black dots denote events included in a cluster. Red lines denote the best linear fits. White and blue “beach balls” denote the composite focal mechanisms for the respective clusters. Black numerical labels below the beach balls indicate the number of events in a cluster. Red numerical labels above the beach balls indicate uncertainty in the estimated strike angle, in degrees.

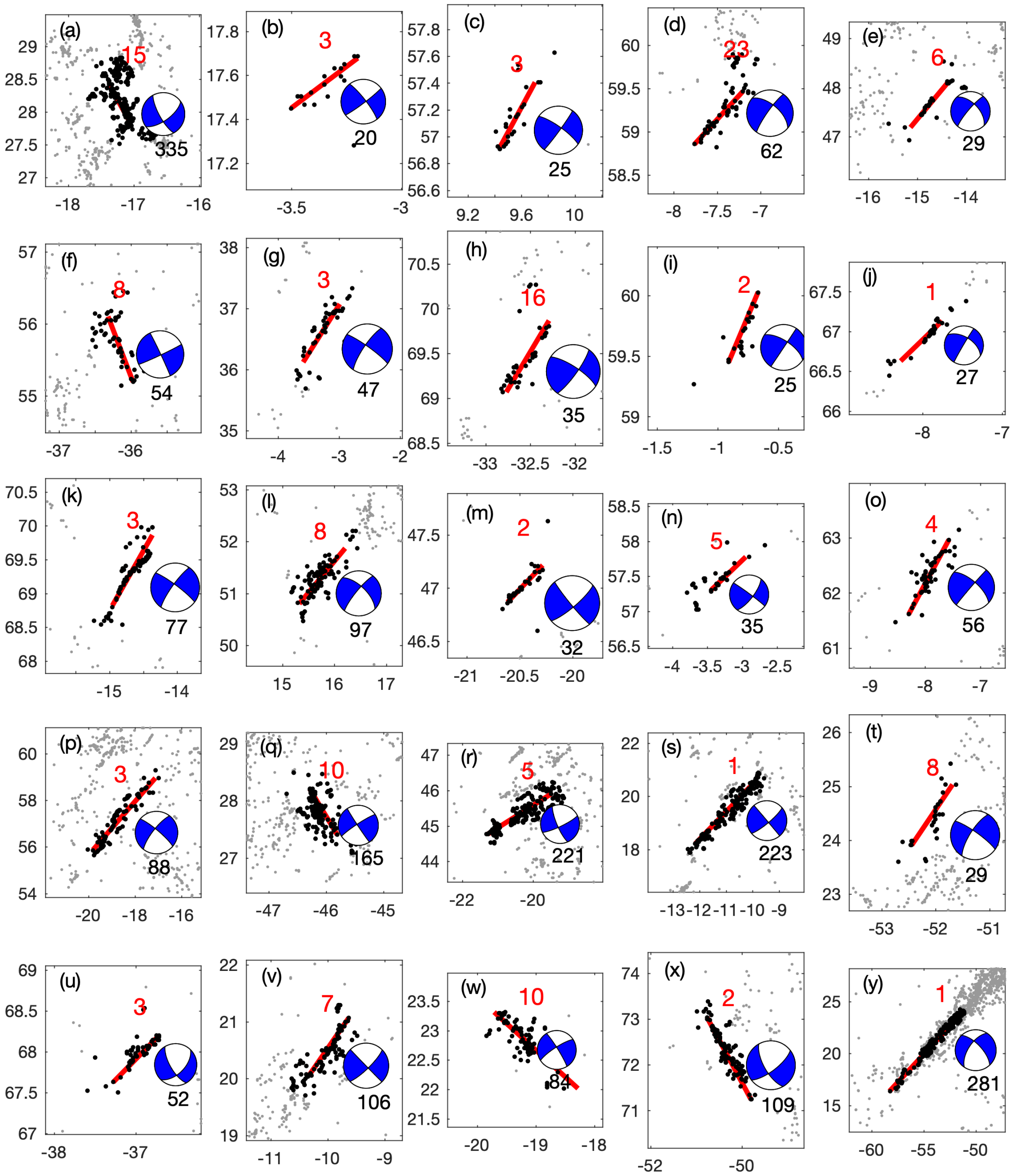

Figure S3: Seismicity lineations identified by the clustering algorithm. Notation is the same as in Figure S2.

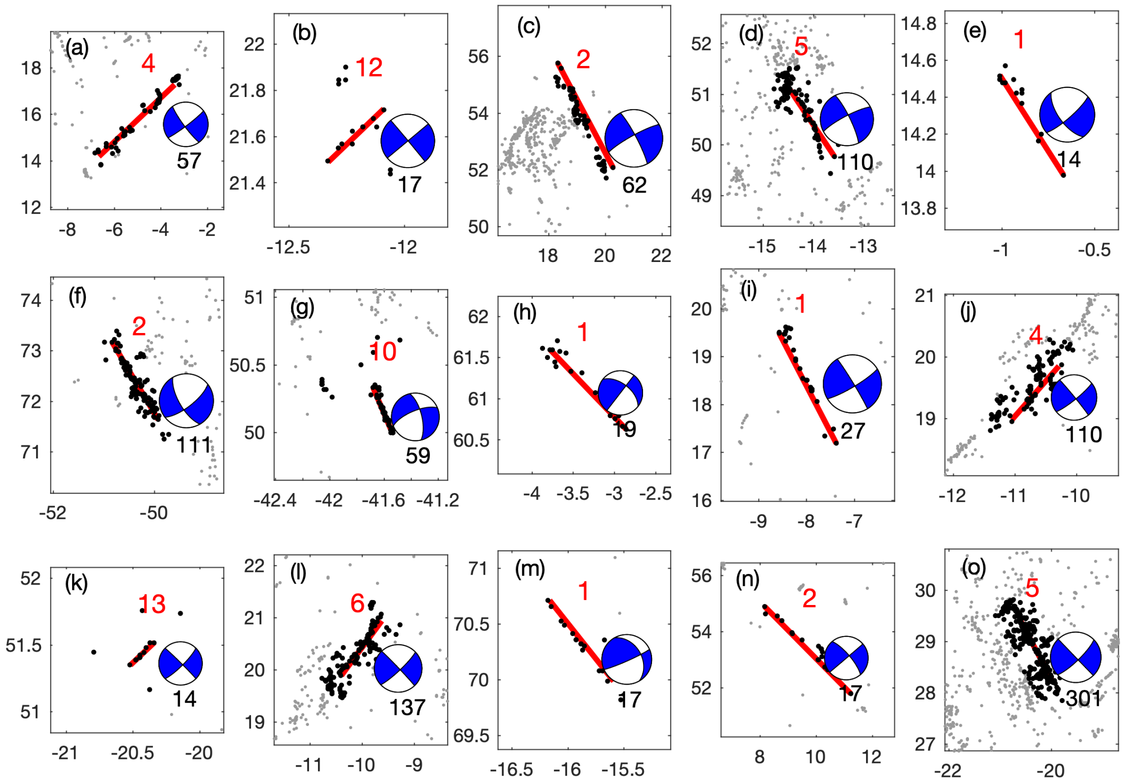

Figure S4: Seismicity lineations identified by the clustering algorithm. Notation is the same as in Figure S2.

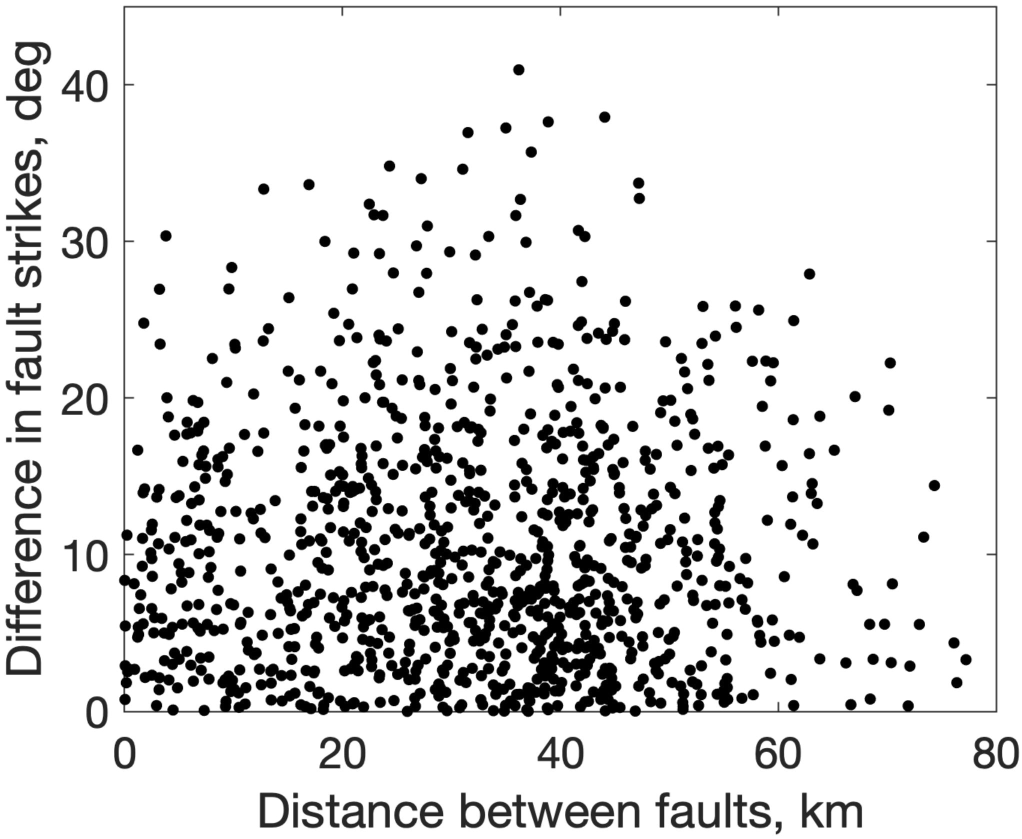

Figure S5: Variability in fault strikes for faults having the same sense of slip, as a function of distance between the faults.

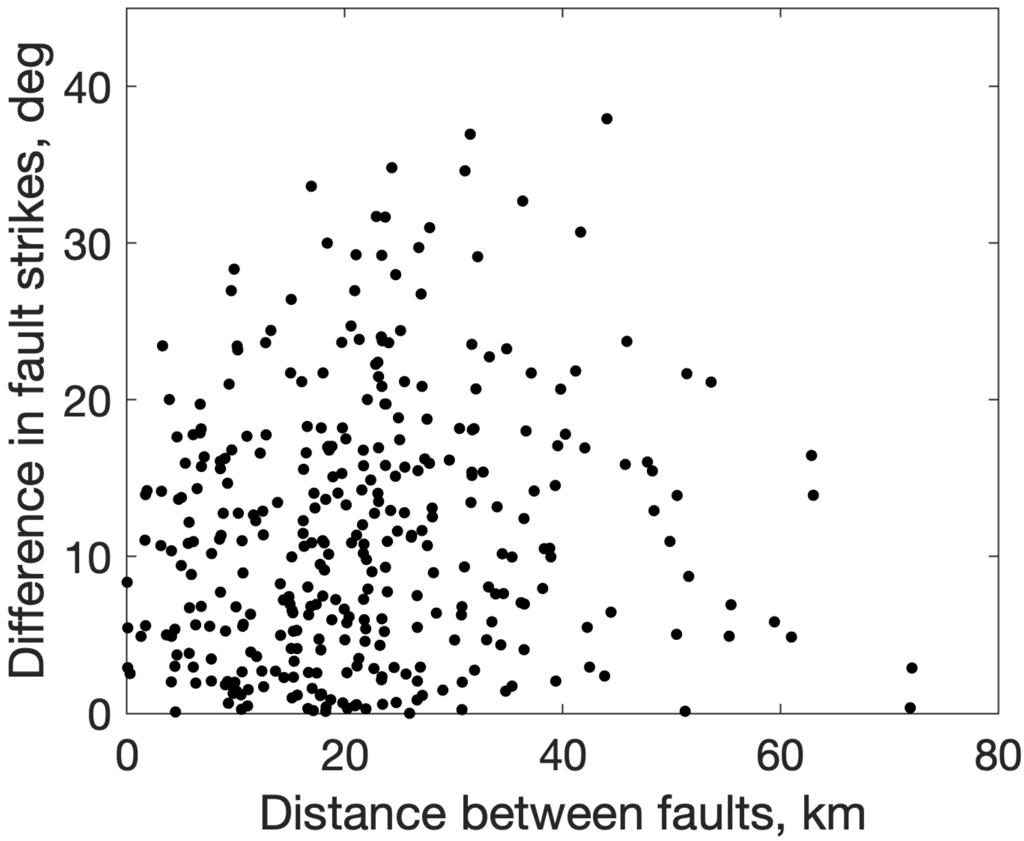

Figure S6: Same as Figure S5, for events with northings > 40 km (see Figure S1a).

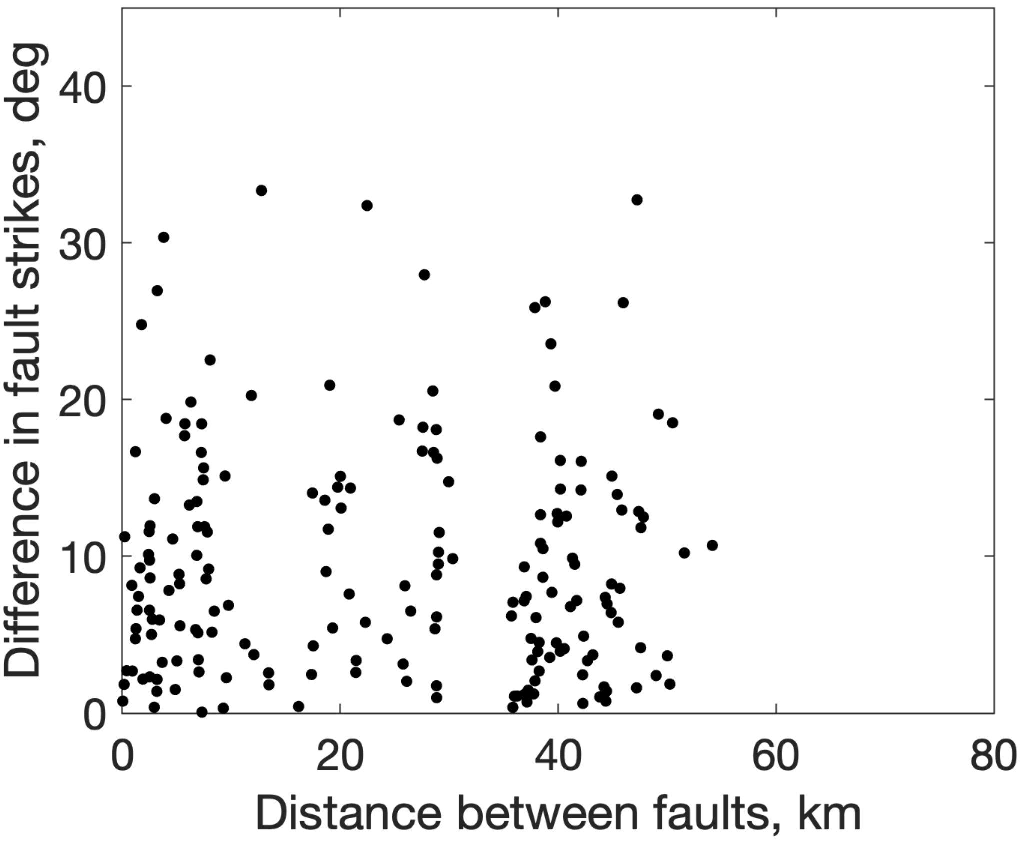

Figure S7: Same as in Figure S5, for events with northings < 40 km (see Figure S1a).

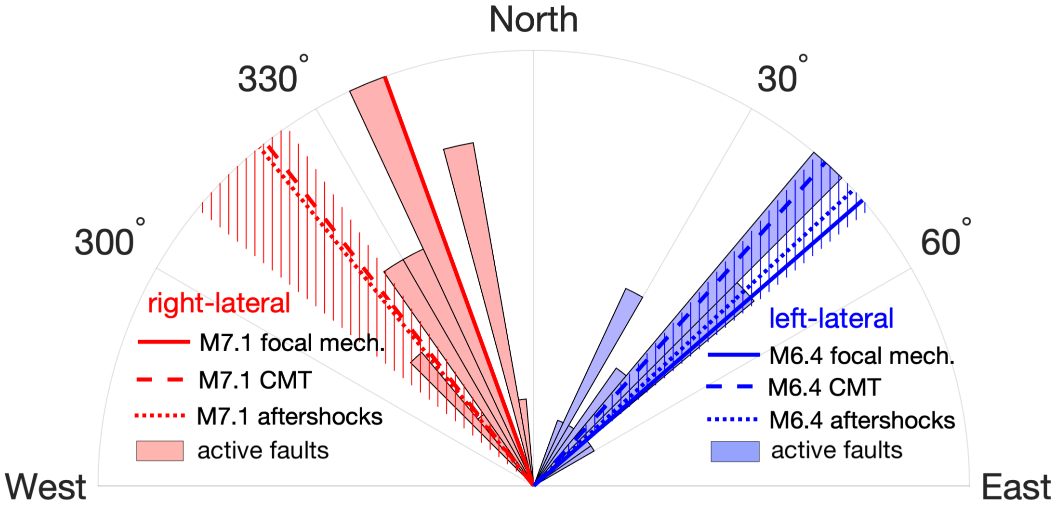

Figure S8: Distribution of strikes for a subset of faults with northings > 40 km (see Figure S1a). Notation is the same as in Figure 2.

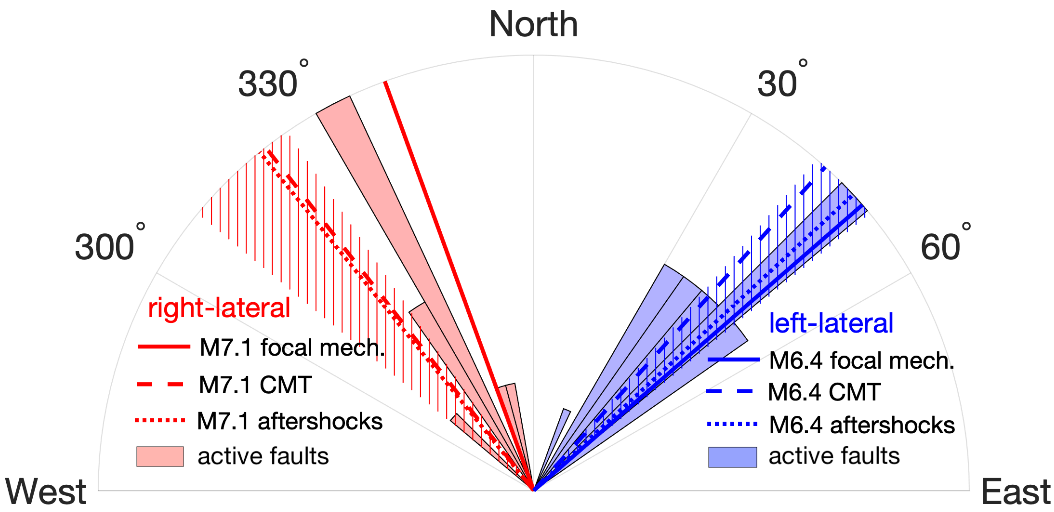

Figure S9: Distribution of strikes for a subset of faults with northings < 40 km (see Figure S1a). Notation is the same as in Figure 2.